frontiers | Frontiers in Earth Science

TYPE Original Research
PUBLISHED 19 January 2023
DOI 10.3389/feart.2023.1105992

OPEN ACCESS

EDITED BY
Meng Wang,
Chang'an University, China

REVIEWED BY
Guangyan Zhou,
China University of Geosciences Wuhan, China
Chao Wang,
Northwest University, China

*CORRESPONDENCE
Jianxin Zhang,
zjx66@yeah.net

SPECIALTY SECTION
This article was submitted to Petrology, a section of the journal Frontiers in Earth Science

RECEIVED 23 November 2022
ACCEPTED 03 January 2023
PUBLISHED 19 January 2023

CITATION
Teng X, Zhang J, Mao X, Wu Y and Guo Q (2023), Geochemistry, zircon U-Pb age and Hf isotope for the Huatugou granitoid in western Qaidam: Petrogenesis and tectonic implications.
Front. Earth Sci. 11:1105992.
doi: 10.3389/feart.2023.1105992

Geochemistry, zircon U-Pb age and Hf isotope for the Huatugou granitoid in western Qaidam: Petrogenesis and tectonic implications

Xia Teng[1,2], Jianxin Zhang[1]*, Xiaohong Mao[1], Yawei Wu[1,2] and Qi Guo[1,2]

[1]Institute of Geology, Chinese Academy of Geological Sciences, Beijing, China, [2]School of Earth and Space Sciences, Peking University, Beijing, China

The Qaidam Precambrian block is located in the northeastern Tibetan Plateau and was intruded by numerous Ordovician-Devonian granitoids during and after the closure of the Proto-Tethys Ocean. In the past 20 years, the granitoids within early Paleozoic subduction-collision belts have been investigated in detail. However, the granitoids intruding the inner part of the Qaidam block, bearing the tectonic significance for the whole block, still need to be understood. This study presents new whole-rock geochemical and zircon U-Pb-Hf isotopic data for the Huatugou granitoids in the Qaidam Precambrian block. The investigated granitoids include granodiorite, monzogranite, biotite granite, and muscovite granite, which intruded the Precambrian basements during 451–400 Ma. The granodiorites (451 ± 6 Ma) display adakitic geochemical features and syn-tectonic textures, and their magmas were generated by the partial melting of the lower mafic crust within a thickened continent. The muscovite granites (410 ± 6 Ma), with negative zircon εHf(t) values of −14.5 to −10.4, were crystallized from fractionated S-type magmas, which were derived from the partial melting of ancient crustal materials. The biotite granite (410 ± 3 Ma) and monzogranites (400 ± 4 Ma) are high-temperature A_2-type granites. The biotite granite displays positive zircon εHf(t) values of +1.7 to +5.6. Its magma was generated by the high-temperature partial melting of juvenile crustal rocks in a thinned lower crust. The monzogranites exhibit higher SiO_2 contents and lower εHf(t) values, and their magmas were derived from the same source but underwent assimilation and fractional crystallization during emplacement. From the thickened to the thinned continent during 451–410 Ma, the western Qaidam block experienced a tectonic transition from compression to extension. Combined with regional geological data, this study suggests that the Qaidam block consisted of the thickened continental crust during subduction processes until the detachment of the subducted slab during the continental collision. The regional extension of the Qaidam block commenced at ~420 Ma, soon after the exhumation of ultrahigh-pressure metamorphic rocks within the northern Qaidam subduction-collision complex belt.

KEYWORDS

Qaidam block, Huatugou granitoids, early paleozoic, zircon U-Pb ages, Hf isotope

1 Introduction

Granitic plutons account for a significant volume of many ancient orogenic belts and have been a primary investigated object concerning orogenic evolution. On the one hand, observations from partial melting experiments indicate that the chemical features of granite products are directly related to melting conditions and source compositions (e.g., Clemens et al., 1986; Patiño Douce, 1995; Winther, 1996; Patiño Douce and Harris, 1998; Castro et al., 1999; Acosta-Vigil et al., 2006), most of which are not exclusively encountered in one specific tectonic setting (Whalen et al., 1987; Eby., 1992; Chappell and White, 2001; Frost et al., 2001; Castillo, 2012). On the other hand, most ancient orogenic belts contain various granitic plutons, each of which was derived from a specific source at different periods of tectonic evolution. In turn, the petrogenesis and formation ages of such a set of various granitoids provide critical constraints on changes in *P-T* conditions and source regions with time, which can be related to a sequential transition of tectonic settings in a relatively well-constrained geological framework (e.g., Zhang et al., 2013; Zhu et al., 2018; Hopkinson et al., 2019).

The Qaidam block, located in the northeastern Tibetan Plateau, is a Precambrian block surrounded by Paleozoic orogenic belts (Zhang et al., 2021). Previous studies indicate that granitic magmas intruding the Qaidam block were mainly crystallized at 470–370 Ma and 270–215 Ma (Wu C. L. et al., 2014b; Cheng et al., 2017; Chen et al., 2020). The early Paleozoic granitic magmatism (470–370 Ma) has been linked to the subduction of the Proto-Tethys Ocean and following collisional to post-collisional processes experienced by the Qaidam block (Wu et al., 2014a; Yu et al., 2019; Yang et al., 2020). This series of tectonic processes also resulted in arc-related magmatism, exhumated high-to ultrahigh-pressure metamorphic associations, and preservation of possible ophiolites (relict of oceanic crust) within the

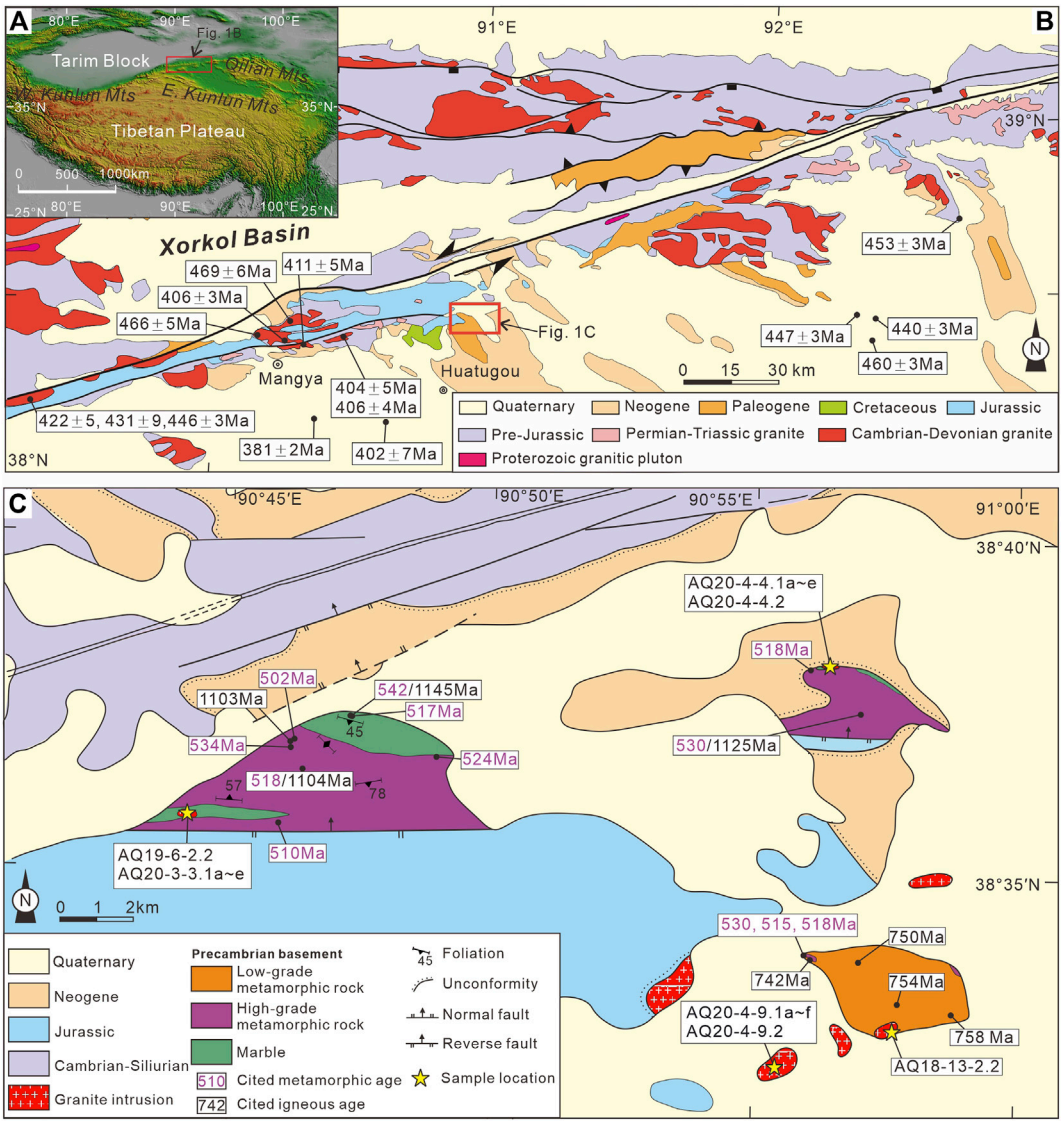

FIGURE 1
(A) Location of the Qaidam basin. **(B)** Simplified western Qaidam geological map (after Cheng et al., 2017). Zircon U-Pb data of early Paleozoic granitoids are cited from Cheng et al. (2017), Wang C. et al., (2014a), and Wu C. L. et al. (2014b). **(C)** Simplified geological map of the study region showing primary lithologies and sample locations. Magmatic and metamorphic zircon U-Pb data are cited from Teng et al. (2020, 2022).

TABLE 1 Sampling location, ICPW norm calculation, and analytic items for granitoids from the western Qaidam block.

No.	Sample no.	Location		Lithology	ICPW norm/wt%				
		Latitude	Longitude		Qtz	Pl	Or	Co	Hy
1	AQ18-13-2.2	38°32′53.44″N	90°57′42.07″E	Biotite granite	22.04	41.52	25.07	0.81	7.76
2	AQ20-4-9.1a	38°32′25.27″N	90°55′35.44″E	Monzogranite	27.40	43.23	22.98	0.34	4.63
3	AQ20-4-9.1b	38°32′25.27″N	90°55′35.44″E		28.34	41.04	23.93	0.62	4.60
4	AQ20-4-9.1c	38°32′25.27″N	90°55′35.44″E		28.57	39.36	25.18	0.86	4.60
5	AQ20-4-9.1d	38°32′25.27″N	90°55′35.44″E		28.57	41.07	23.58	0.69	4.62
6	AQ20-4-9.1e	38°32′25.27″N	90°55′35.44″E		29.36	38.64	24.96	0.94	4.63
7	AQ20-4-9.1f	38°32′25.27″N	90°55′35.44″E		29.70	41.11	22.33	0.78	4.62
8	AQ20-4-9.2	38°32′25.27″N	90°55′35.44″E		26.82	35.29	31.61	0.07	4.57
9	AQ19-6-2.2	38°36′2.17″N	90°44′21.65″E	Muscovite granite	30.96	29.33	35.11	2.03	1.77
10	AQ20-3-3.1a	38°36′2.31″N	90°44′27.04″E		32.56	31.73	29.91	2.77	2.19
11	AQ20-3-3.1b	38°36′2.31″N	90°44′27.04″E		34.74	33.23	28.22	1.60	1.51
12	AQ20-3-3.1c	38°36′2.31″N	90°44′27.04″E		30.52	31.47	33.77	1.60	1.80
13	AQ20-3-3.1d	38°36′2.31″N	90°44′27.04″E		28.35	29.09	38.47	1.43	1.84
14	AQ20-3-3.1e	38°36′2.31″N	90°44′27.04″E		34.29	32.79	28.90	1.83	1.55
15	AQ20-4-4.1a	38°38′11.93″N	90°56′41.88″E	Granodiorite	33.65	50.89	10.36	1.41	2.95
16	AQ20-4-4.1b	38°38′11.93″N	90°56′41.88″E		33.25	51.07	10.46	1.41	3.03
17	AQ20-4-4.1c	38°38′11.93″N	90°56′41.88″E		33.13	51.13	10.93	1.20	2.90
18	AQ20-4-4.1d	38°38′11.93″N	90°56′41.88″E		33.01	50.51	11.41	1.24	3.06
19	AQ20-4-4.1e	38°38′11.93″N	90°56′41.88″E		32.49	52.36	10.08	1.25	3.10
20	AQ20-4-4.2	38°38′13.55″N	90°56′30.93″E		33.32	50.83	10.61	1.27	3.20

Qtz, Quartz; Pl, Plagioclase; Or, Orthoclase; Co, Corundum; Hy, Hypersthene.

northern Qaidam and northern East Kunlun (southern Qaidam) subduction-collision belts (Zhang et al., 2017; Dong et al., 2018; Song et al., 2018 and references therein). In the past 20 years, most investigated granitoids, especially syn-collisional granitoids, came from subduction-collision belts, which are complex belts resulting from processes including continental subduction, collision, exhumation of subducted crust, and post-collisional extension. In addition to the complexity of interpreting the petrogenesis, the tectonic processes, inferred from granitoids within subduction-collision belts, hardly reflect the response of the whole Qaidam block, which used to be a Precambrian micro-continent located on the margin of East Gondwana (Teng et al., 2020; Zhang et al., 2021; Teng et al., 2022). Recognizing the early Cambrian ultrahigh-temperature (UHT, >900°C) metamorphism within western Qaidam provides new constraints on the paleo-geographic position of the Qaidam block (Teng et al., 2020), a continent arc of the Gondwana facing the Proto-Tethys Ocean, before early Paleozoic subduction-collision. Meanwhile, it also evokes a tectonic interest in granitic intrusions in the same region in the Precambrian Qaidam block. It is recognized that the western Qaidam was affected by Ordovician-Devonian felsic magmatism, inferred from 469 to 381 Ma granitoids along the Altyn Tagh Fault and in drills (Figure 1B; Cheng et al., 2017; Wang C. et al., 2014a; Wu C. L. et al., 2014b). However, the tectonic transitions during the prolonged felsic magmatism in western Qaidam, a part of the Precambrian micro-continent, have not been well constrained.

This study presents whole-rock geochemical and zircon U-Pb-Hf isotopic data for Huatugou granitoids, which were emplaced into the UHT metamorphic rocks-bearing Precambrian basements (Figure 1C). Our new data not only put new constraints on the ages, sources, and petrogenesis of these granitoids but also provide essential insights into the tectonic processes of the whole Qaidam block.

2 Geological setting and sampling

2.1 Geological setting

The Qaidam Basin, located in the northeastern Tibetan Plateau, is bounded by the Qilian Mountains to the northeast, the Altyn Tagh Mountains to the northwest, and the East Kunlun Mountains to the south (Figure 1A). The main body of the Qaidam basement is covered by thick Mesozoic-Cenozoic sediments. Hence, the nature of the basement is mainly studied with outcrops and drills on the basin's margins.

The Paleoproterozoic basement of the Qaidam block, Jinshuikou Group, comprises migmatite, gneiss, amphibolite, schist, quartzite,

and marble and is mainly exposed in the south of the Qaidam Basin (Wang et al., 1983). During early Neoproterozoic, the Jinshuikou Group, as well as some Mesoproterozoic protoliths in the northern Qaidam (the northeast of the Qaidam Basin), underwent a series of high-grade metamorphism, which is characterized by transitions from Buchan-type (low-pressure) metamorphism at ~1.0 Ga to Barrovian-type up to high-pressure granulite-facies metamorphism at 0.94–0.92 Ga (Ren et al., 2019; He et al., 2020; Ren et al., 2021; He et al., 2022). Coeval magmatism produced abundant S-type granites, whose emplacements started as early as ~1.1 Ga and widely occurred during 1.0–0.9 Ga (He et al., 2016; He et al., 2018; Teng et al., 2022 and references therein). The 1.1–0.9 Ga metamorphism and magmatism resulted from prolonged subduction-collision and were followed by 0.85–0.75 Ga felsic and mafic magmatism in a continental rifting setting, linked to the assembly and breakup of the Rodinia supercontinent, respectively (Song et al., 2010; Yu et al., 2013; Ren et al., 2021; He et al., 2022; Teng et al., 2022).

During the early Paleozoic, the Qaidam block underwent continental subduction-collision following the closure of the Proto-Tethys Ocean, as implied by arc-related Tanjianshan Group metavolcanic rocks and gabbro dikes (514–465 Ma, Wu et al., 1987; Li et al., 1999; Yuan et al., 2002; Shi et al., 2004) and subduction-related (U)HP metamorphic rocks (457–422 Ma, Song et al., 2005; Yang et al., 2005; Mattinson et al., 2006; Chen et al., 2009; Zhang et al., 2010; Meng et al., 2013; Song et al., 2018) within the northern and southern Qaidam. In northern Qaidam (the northeast of the Qaidam Basin), granitic magma emplacement started as early as ~470 Ma in a continental arc setting, prevailed at 446–397 Ma during the exhumation of subducted crust, and continued to 382–372 Ma in a post-collisional environment (Wu et al., 2014a; Sun et al., 2020; Yang et al., 2020). In the southern Qaidam (including the northern East Kunlun), Paleozoic magmatism primarily occurred during 424–394 Ma in a post-collisional extension, forming granitic plutons (Zhang et al., 2003; Chen et al., 2006; Cheng et al., 2017; Chen et al., 2020), mafic-ultramafic intrusions (Wang G. et al., 2014b; Peng et al., 2016; Song et al., 2016), and rhyolitic rocks of the Maoniushan Formation (Lu et al., 2010). In addition, the western Qaidam, to the south of the active left-slip Altyn Tagh Fault, was also affected by Ordovician-Devonian felsic magmatism, inferred from 469 to 381 Ma granitoids along the Altyn Tagh Fault and in drills (Figure 1B; Cheng et al., 2017; Wang C. et al., 2014a; Wu C. L. et al., 2014b).

The rock records regarding geological activities of the Qaidam block between 750 and 520 Ma are mainly found in the western Qaidam. Exposed in the north of Huatugou City, the Precambrian basements of western Qaidam consist of granulite-facies metamorphic rocks and low-grade metamorphic supracrustal rocks (Figure 1C). The Huatugou granulite-facies rocks include felsic gneisses with protolith ages of ~1.1 Ga (Teng et al., 2022), pelitic gneisses, and olivine-bearing marbles, with minor Mg-Al granulite and mafic granulite lenses. They experienced early Cambrian (540–500 Ma) UHT metamorphism, which is characterized by a clockwise *P-T* path with a prograde *P* peak >1.4 GPa (Teng et al., 2020). The UHT metamorphism was thought to occur within the Kuunga Orogen; hence, the Qaidam block was located on the margin of East Gondwana (Teng et al., 2020; Teng and Zhang, 2020). The low-grade metamorphic supracrustal association comprises metavolcanic rocks, quartzofeldspathic leptynite, mica schist, and quartzite. The protoliths of felsic metavolcanic rocks were crystallized from high-temperature A-type magmas with positive zircon εHf(t) values (+0.9 to +6.1), which were emplaced in a continental rifting environment at ~0.75 Ga (Teng et al., 2022). Both high-grade and low-grade metamorphic basements exposed in the Huatugou area were intruded by granitic plutons and dikes (Figure 1C), whose petrogenesis and tectonic significance are the focus of this study.

2.2 Sampling

In the Huatugou area, the granitoids mainly occurred as small plutons and dikes intruding Precambrian basements (Figure 1C). In this study, investigated granitoids include biotite granite, monzogranite, muscovite monzogranite, and granodiorite. A total of 20 samples were used for whole-rock geochemical analyses, and four representative samples were selected for zircon U-Pb age and Hf isotope analyses (Table 1).

The biotite granite, sample AQ18-13-2.2, was collected from a dike, which is 1–5 m wide and intruded mylonitic quartzite (Figure 2A). The sample consists of plagioclase (40%–45%), K-feldspar (20%–25%), quartz (20%–25%), biotite (7%–10%), and amphibole (1%–3%) (Figure 2B). The monzogranite samples AQ20-4-9.1a~f and AQ20-4-9.2 were collected from a granitic pluton that was broken into fragments widespread the hills and buried by the sediments (Figure 2C). Monzogranites are fine-to coarse-grained and composed of K-feldspar (20%–30%), plagioclase (35%–45%), quartz (25%–30%), biotite (1%–3%), and muscovite (<1%) (Figure 2D). The muscovite granites, including samples AQ19-6-2.2 and AQ20-3-3.1a~e, were collected from a granitic dike, which is ~20 m wide and intruded marble (Figures 1C, 2E). Muscovite granites consist of K-feldspar (28%–33%), plagioclase (30%–35%), quartz (30%–35%), muscovite (5%–7%), and biotite (~1%). Muscovite and plagioclase are deformed and aligned under the microscope (Figure 2F). The granodiorite samples (AQ20-4-4.1a~e and AQ20-4-4.2) were collected from a granitic pluton intruding marble near a talc deposit (Figure 1C). Granodiorites exhibit porphyritic textures and are locally mylonitized in the contacting zone with marble (Figure 2G). Granodiorites mainly consist of plagioclase (50%–55%), quartz (30%–35%), K-feldspar (9%–12%), and biotite (~3%). The phenocrysts consist of K-feldspar and plagioclase, while quartz mainly occurs in the matrix (Figure 2H).

3 Analytical methods

3.1 Whole-rock major and trace elemental analysis

The whole-rock composition analysis was conducted at the Wuhan Samplesolution Analytical Technology Co., Ltd., China. The major elements were measured by a Primus II X-ray fluorescence spectrometer (XRF). The trace elements were measured by an Agilent 7700e inductively coupled plasma mass spectrometry (ICP-MS). The analytical uncertainties are ~5%.

3.2 Zircon U-Pb isotopic and trace elemental analysis

Zircon grains were extracted from pulverized rock samples using combined heavy liquid and magnetic techniques and handpicked

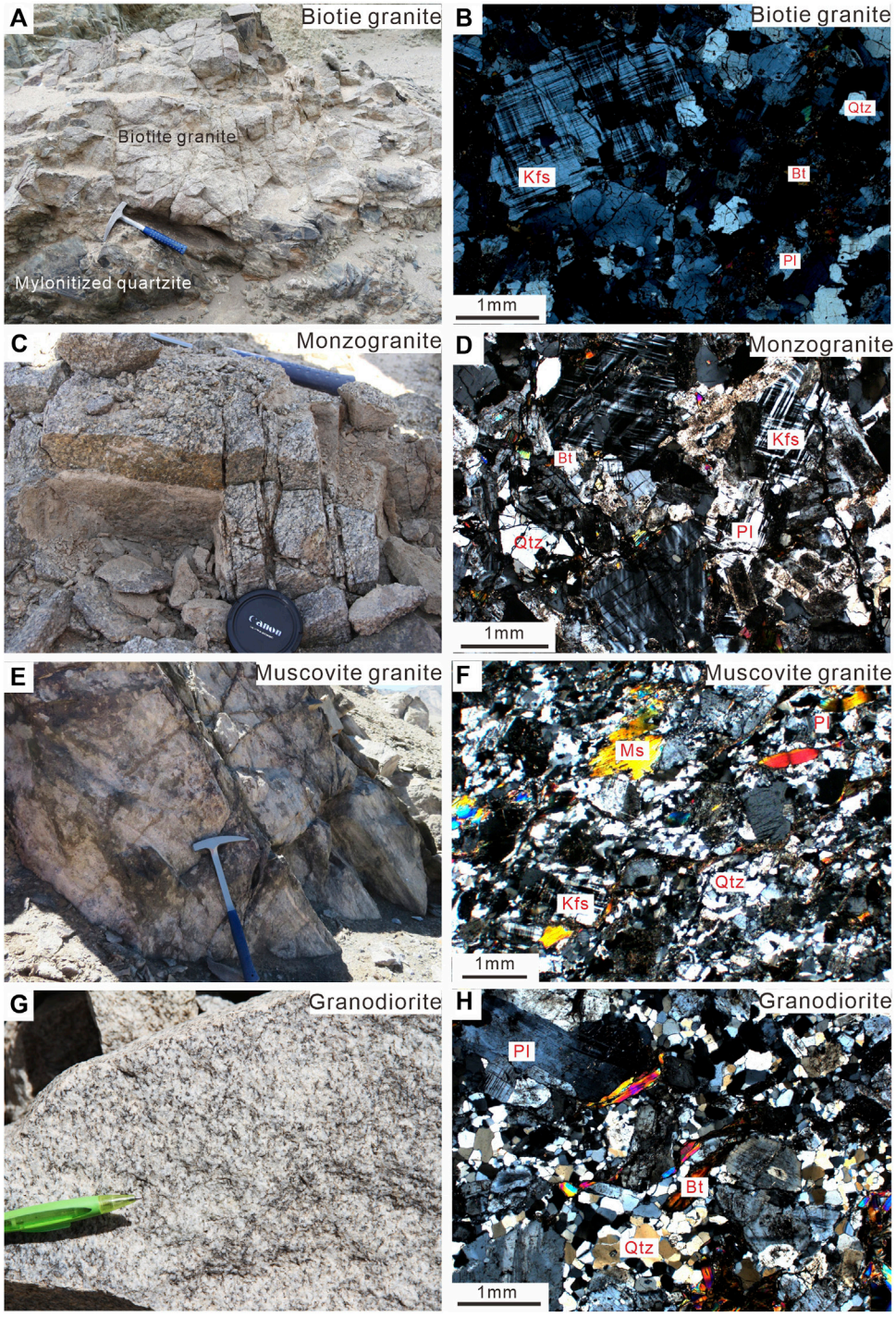

FIGURE 2
Field photographs and photomicrographs of **(A,B)** biotite granite, **(C,D)** monzogranite, **(E,F)** muscovite granite, and **(G,H)** granodiorite in the Huatugou area. Bt, biotite; Kfs, K-feldspar; Ms, muscovite; Pl, plagioclase; Qtz, quartz.

under a binocular microscope. Separated zircon grains were mounted in an epoxy resin and polished to expose about half the grains. Cathodoluminescence (CL) images were taken using an FEI PHILIPS XL30 SFEG scanning electron microscope (SEM) at the Institute of Geology, Chinese Academy of Geological Sciences (CAGS). Zircon U-Pb isotope and trace element concentrations were measured by an Analytikjena PQMS Elite ICP-MS equipped with a RESOlution 193 nm laser ablation system at Beijing Createch Testing Technology Co., Ltd. The laser spot was set to 24 μm with a repetition rate of 6 Hz and an energy density of 6 J/cm^2. Zircon standards GJ-1 (602 Ma, Jackson et al., 2004), 91500 (1065 Ma, Wiedenbeck et al., 1995), and Plesovice (337 Ma, Sláma et al., 2008) were analyzed together with samples for quality control of zircon U-Pb isotope data. Each measurement consisted of a 15 s background signal acquisition followed by a 45 s data acquisition from the samples. Off-line raw data selection, background and

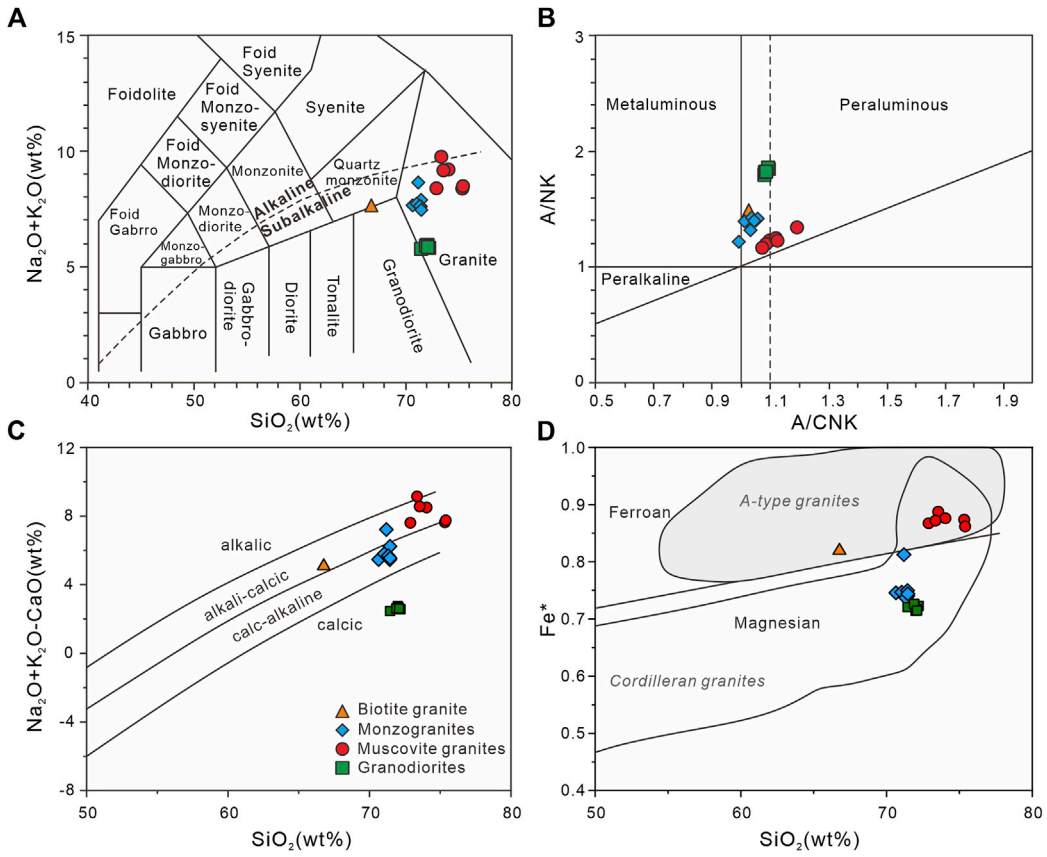

FIGURE 3
Geochemical classification diagrams using major element oxides. **(A)** (Na_2O+K_2O) *vs.* SiO_2 (Irvine and Baragar, 1971; Middlemost, 1994). **(B)** A/NK *vs.* A/CNK (Maniar and Piccoli, 1989). A/CNK = molar $Al_2O_3/(CaO+Na_2O+K_2O)$; A/NK = molar $Al_2O_3/(Na_2O+K_2O)$. **(C)** (Na_2O+K_2O-CaO) *vs.* SiO_2 and **(D)** FeO* *vs.* SiO_2 (Frost et al., 2001). Fe*=$FeO^T/(FeO^T+MgO)$.

analyzed signals integration, time-drift correction, and quantitative calibration for U-Pb dating were performed using ICPMSDataCal (Liu et al., 2010). U-Pb concordia plots and weighted mean $^{206}Pb/^{238}U$ age calculations were conducted using Isoplot 4.15 (Ludwig, 2012). Uncertainty of individual analysis was reported with a 1σ error, and weighted mean ages were calculated at a 95% confidence level. Trace element concentrations were corrected using NIST610 as an external and Si as an internal standard.

3.3 Zircon Hf isotopic analysis

Hf isotope compositions of the dated zircons were measured using a Neptune Plus ICP-MS (Thermo Fisher Scientific, Germany) in combination with a Geolas HD excimer ArF laser ablation system (Coherent, Germany) at the Wuhan Samplesolution Analytical Technology Co., Ltd., China. All data were acquired with a beam size of 44 μm, a laser repetition rate of 8 Hz, and an energy density of 10 J/cm^2. The zircon 91500, GJ-1, and Plesovice were used as external standards and have weighted mean $^{176}Hf/^{177}Hf$ values of 0.2822939 ± 0.0000093, 0.282008 ± 0.000022, and 0.2824780 ± 0.0000049, respectively. Offline selection, background and analyzed signals integration, and mass calibration were performed using ICPMSDataCal (Liu et al., 2010). All calculated data were considered for isobaric interferences and normalized to $^{179}Hf/^{177}Hf$ of 0.7325 using an exponential correction for mass bias.

4 Results

4.1 Whole-rock geochemistry

Whole-rock compositions are presented in Supplementary Table S1 and illustrated in Figures 3, 4. The biotite granite has 66.77 wt% SiO_2, 7.62 wt% total alkali (Na_2O+K_2O), 2.53 wt% CaO, 15.19 wt% Al_2O_3, 4.68 wt% $Fe_2O_3^T$, and 0.93 wt% MgO, with high FeO^T/MgO (4.21) and Fe* [=$FeO^T/(FeO^T+MgO)$=0.82]. In the classification diagram, the biotite granite falls on the boundary between quartz monzonite and granodiorite (Figure 3A). In discrimination diagrams of A/NK *vs.* A/CNK, (Na_2O+K_2O-CaO) *vs.* SiO_2, and Fe* *vs.* SiO_2 (Figures 3B–D), the biotite granite falls in weakly peraluminous, alkali-calcic, and ferroan fields. The biotite granite contains 367 ppm REE. In the chondrite-normalized REE diagram, it displays LREE enrichment relative to HREE [$(La/Yb)_N$=12.64] and a negative Eu anomaly ($Eu/Eu^*=Eu_N/(Sm_N\times Gd_N)^{1/2}$ =0.49) (Figure 4A). In the primitive mantle-normalized diagram, the biotite granite exhibits enrichments of Th, La, Nd, and Zr and depletions of Ba, Nb, Ta, and Sr (Figure 4B).

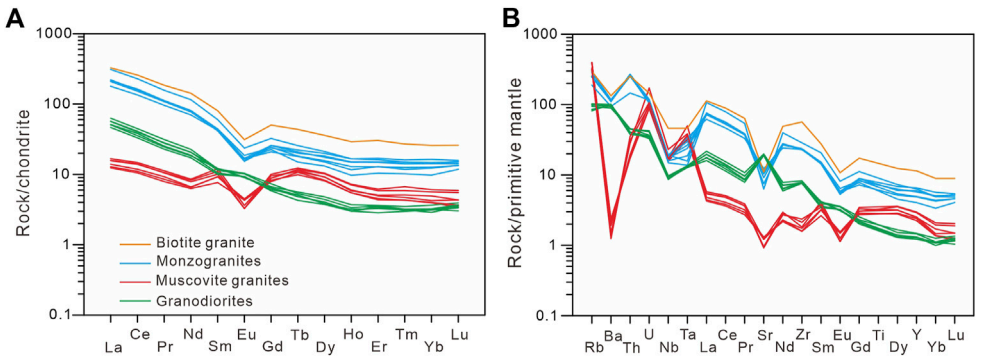

FIGURE 4
(A) Chondrite-normalized rare Earth elements (REE) diagram and **(B)** Primitive-mantle normalized trace element diagram for investigated Huatugou granitoids. Chondrite and Primitive-mantle reference values are from Sun and McDonough (1989).

The monzogranites have 70.64–71.46 wt% SiO_2, 7.43–8.60 wt% total alkali, 1.39–2.15 wt% CaO, 13.59–14.58 wt% Al_2O_3, 2.37–2.74 wt % $Fe_2O_3^T$, and 0.57–0.76 wt% MgO, with 0.74–0.81 for Fe*. In the geochemical classification diagrams (Figure 3), all monzogranite samples are plotted in the magnesian granite field, and most of them exhibit weekly peraluminous and calc-alkaline characteristics. Total REE contents of monzogranites vary from 192 to 312 ppm. In the chondrite-normalized REE diagram, monzogranites show LREE enrichments relative to HREE [$(La/Yb)_N$=11–23], with notably negative Eu anomalies (Eu/Eu*=0.48–0.57) (Figure 4A). In the primitive mantle-normalized diagram, they show enrichments of Th, La, and Nd and depletions of Ba, Nb, Ta, and Sr (Figure 4B).

The muscovite granites contain 72.89–75.40 wt% SiO_2, 8.34–9.71 wt% total alkali, 0.57–0.75 wt% CaO, 13.54–14.63 wt% Al_2O_3, 0.94–1.35 wt% $Fe_2O_3^T$, and 0.12–0.15 wt% MgO, with high Fe* (0.86–0.89). In the classification diagrams (Figure 3), the muscovite granites fall in the granite area and display peraluminous, ferroan, and alkali-calcic to alkalic characteristics. In the chondrite-normalized diagram (Figure 4A), the muscovite granites exhibit low REE contents (21–27 ppm) and flat REE patterns [$(La/Yb)_N$=3–4], with notably negative Eu anomalies (Eu/Eu*=0.32–0.56). In the Primitive mantle-normalized diagram (Figure 4B), the muscovite granites show depletions of Ba, Nb, Sr, Zr, and Eu and enrichments of Rb, U, Ta, and Sm.

The granodiorites have 71.46–72.20 wt% SiO_2, 5.75–5.93 wt% total alkali, 3.18–3.29 wt% CaO, 15.66–15.94 wt% Al_2O_3, 1.35–1.50 wt% $Fe_2O_3^T$, and 0.49–0.54 wt% MgO, with the Fe* of 0.71–0.73. According to classification diagrams (Figure 3), all granodiorite samples belong to granites of peraluminous, calc, and ferroan series. The granodiorites contain 47–62 ppm REE. In the chondrite-normalized REE diagram (Figure 4A), they exhibit LREE enrichments relative to HREE [$(La/Yb)_N$=15–20] with weekly positive Eu anomalies (Eu/Eu*=1.02–1.21). The Primitive mantle-normalized diagram shows that they are enriched in Ba, La, Sr, and Zr and depleted in Nb (Figure 4B).

4.2 Zircon U-Pb geochronology

Representative zircon CL images are presented in Figure 5. Zircon geochronological data are presented in Supplementary Table S2 and illustrated in Figure 6. Zircons in biotite granite (AQ18-13-2.2) and monzogranite (AQ20-4-9.2) are euhedral, 100–220 μm in length with length/width ratios of 2:1 to 3:1 (Figures 5A, B). In CL images, most zircons exhibit clear oscillatory zoning, which is interrupted by irregularly patchy zones in some monzogranite zircons (Figure 5B). Zircons from the biotite granite contain 36–492 ppm Th and 66–559 ppm U, with Th/U ratios of 0.43–0.96 (Supplementary Table S2). Twenty-nine of 30 analyses yield $^{206}Pb/^{238}U$ ages of 432–393 Ma, with a weighted mean $^{206}Pb/^{238}U$ age of 410 ± 3 Ma (MSWD=2.9) (Figure 6A). Twenty-two zircons were analyzed for the monzogranite and had 59–531 ppm Th and 102–1029 ppm U, with Th/U ratios varying from 0.32 to 1.47 (Supplementary Table S2). Except for one inherited zircon, the remaining 21 zircons yield $^{206}Pb/^{238}U$ ages of 414–382 Ma, with a weighted mean $^{206}Pb/^{238}U$ age of 400 ± 4 Ma (MSWD=3.9) (Figure 6C). In the chondrite-normalized REE diagram (Figures 6B, D), biotite granite and monzogranite zircons exhibit HREE enrichments relative to LREE, with positive Ce anomalies and negative Eu anomalies.

The muscovite granite (AQ19-6-2.2) contains zircons with 30–80 μm in length and length/width ratios of 1:1 to 2:1. In CL images, zircons exhibit oscillatory or sector zoning; some zircons contain inherited cores with relatively dark-CL luminance (Figure 5C). Twenty analyzed zircons have 25–444 ppm Th and 70–418 ppm U with Th/U ratios of 0.27–1.06, and their $^{206}Pb/^{238}U$ ages vary from 393 to 455 Ma. Except for two inherited zircons (Figure 5C), the rest 18 analyzed zircons yield a weighted mean $^{206}Pb/^{238}U$ age of 410 ± 6 Ma (MSWD=5.7) (Figure 6E). The chondrite-normalized REE diagram displays that the muscovite granite zircons are enriched in HREE relative to LREE with notably positive Ce anomalies (Figure 6F).

Zircons from the granodiorite (AQ20-4-4.2) are 60–160 μm in length with length/width ratios of 3:2 to 3:1. CL images show that most zircons are oscillatory-zoned, and many of them are either mantled by dark rims or contain fragmental cores (Figure 5D). Among 28 analyzed spots, twelve spots were ignored owing to high discordance. Four analyses on inherited cores yield $^{206}Pb/^{238}U$ ages of 1632–509 Ma (Supplementary Table S2). The remaining 12 analyses on oscillatory-zoned zircons yield $^{206}Pb/^{238}U$ ages of 470–441 Ma, with a weighted mean $^{206}Pb/^{238}U$ age of 451 ± 6 Ma (MSWD=4.0) (Figure 6G). These zircons contain 70–394 ppm Th and 229–1344 ppm U with variable Th/U ratios (0.07–0.40) and highly scattered chondrite-normalized REE patterns (Figure 6H).

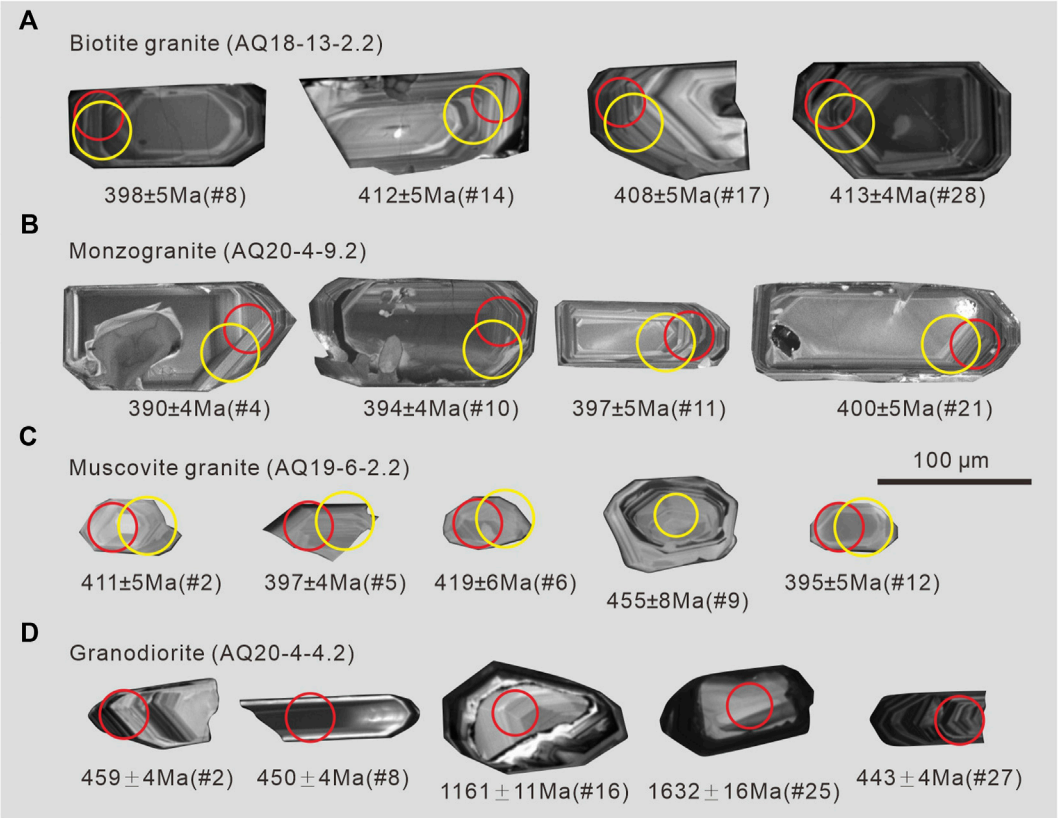

FIGURE 5
(A–D) Cathodoluminescence (CL) images of investigated granitic zircons. The red and yellow circles indicate the locations of U-Pb dating and Hf isotopic analyses.

4.3 Zircon Hf isotopes

The zircon Hf isotopic data are presented in Supplementary Table S3 and illustrated in Figure 7. For the biotite granite (AQ18-13-2.2), zircon $^{176}Hf/^{177}Hf$ ratios are 0.282574–0.282688. Zircons exhibit the initial εHf(t) values of +1.7 to +5.6 (at 410 Ma) and Hf two-stage model ages (T_{DM2}) of 1293–1042 Ma (Figure 7). The monzogranite (AQ20-4-9.2) zircons have $^{176}Hf/^{177}Hf$ ratios of 0.282497–0.282581 and εHf(t) values of −2.0 to +1.8 at 400 Ma. Their T_{DM2} ages vary from 1520 to 1280 Ma. Zircons from the muscovite granite (AQ19-6-2.2) display $^{176}Hf/^{177}Hf$ ratios of 0.282119–282230 and εHf(t) values of −14.5 to −10.4 (at 410 Ma), with T_{DM2} ages of 2317–2058 Ma.

5 Discussion

5.1 Petrogenesis

5.1.1 Biotite granite and monzogranites

The biotite granite displays similar chemical features to A-type granites (Figure 8A, B; Whalen et al., 1987), including high contents of total alkali (7.62 wt%), $Fe_2O_3^T$ (4.68 wt%), highly charged cations (Nb, Y, Zr, REE), and high ratios of FeO^T/MgO (4.54) and 10000Ga/Al (3.06), but low CaO (2.53 wt%). In addition, the high Fe* (0.82) of biotite granite also indicates an A-type affinity (Figure 3D; Frost et al., 2001). Although there is no alkaline mineral, such as arfvedsonite and riebeckite, the high zircon saturation temperature (908°C) was obtained for the biotite granite using the zircon solubility model of Watson and Harrison (1983). In the absence of inherited zircons, the calculated temperature reflects the magma temperature. Therefore, the biotite granite was formed by a high-temperature melting process, similar to A-type granites (Collins et al., 1982; Clemens et al., 1986; Whalen et al., 1987; Chappell and White, 2001).

Similar to the biotite granite, the monzogranites sampled nearby exhibit high total alkali (7.43–8.6 wt%), $Fe_2O_3^T$ (2.37–2.74 wt%), and Fe*(0.74–0.81), and low CaO (1.39–2.15 wt%). In addition, the monzogranites and biotite granite share similar distribution patterns for trace elements and Hf isotopic compositions (Figures 4, 7), implying that they were derived from the same source. The Ga/Al ratios in the biotite granite and monzogranites decrease with decreasing Zr, consistent with the chemical trend of A-type granite fractionation (Wu et al., 2017). In comparison with the biotite granite, the monzogranites have higher SiO_2 and lower CaO, $Fe_2O_3^T$, MgO, Al_2O_3, Zr, and total REE contents with lower εHf(t) values (Figures 7, 9), which likely resulted from an assimilation and fractional crystallization (AFC) process. For instance, the assimilation of upper-crustal materials would decrease the εHf(t) values of ascending magma. The decreases in CaO and Al_2O_3 with increasing SO_2 could result from the fractionation of feldspar and decreases in $Fe_2O_3^T$ and MgO from the fractionation of biotite (Figure 10A). The fractionation of zircon, as well as monazite and apatite (Figure 10B), would decrease Zr and total REE contents.

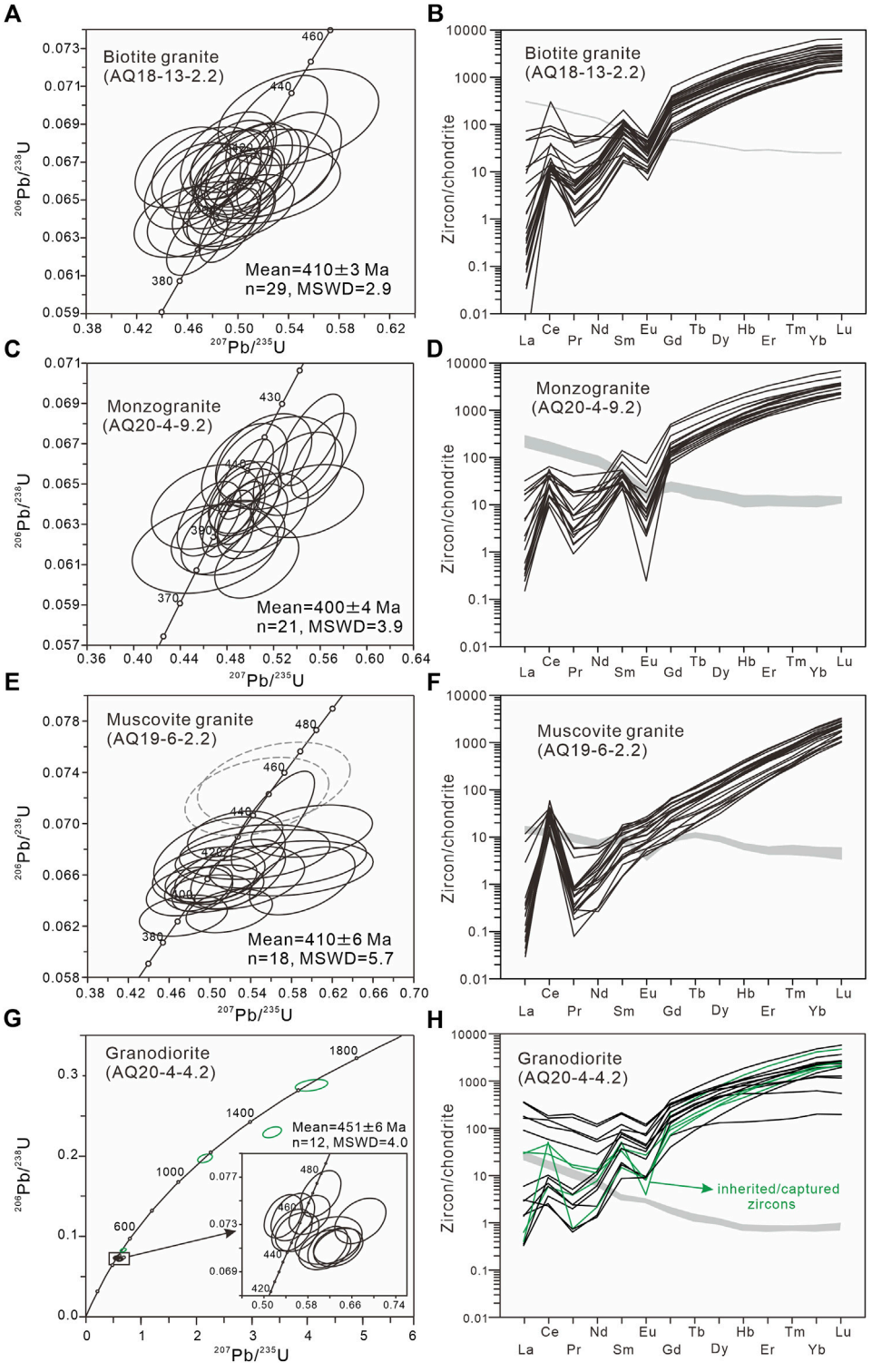

FIGURE 6
Zircon U-Pb concordia diagrams and chondrite-normalized REE diagrams for **(A,B)** biotite granite, **(C,D)** monzogranite, **(E,F)** muscovite granite, and **(G,H)** granodiorite in the Huatugou area. The whole-rock REE patterns in Figure 3A are gray-shaded here.

The least fractionated sample (biotite granite) shows depletions of Eu and Sr and the enrichment of Y (Figure 4), suggesting that plagioclase (instead of garnet) is stable in the source region, consistent with a low-pressure melting condition. The biotite granite has Yb/Ta and Y/Nb ratios of 2.3 and 1.6, similar to continental crust (Taylor and McLennan, 1995). Biotite granite and monzogranites are chemically classified into the A_2 group (Figures 8C, D), which represents magmas generated by the remelting of the continental crust or underplated crust that was initially formed during subduction or continent-continent collision (Eby, 1992).

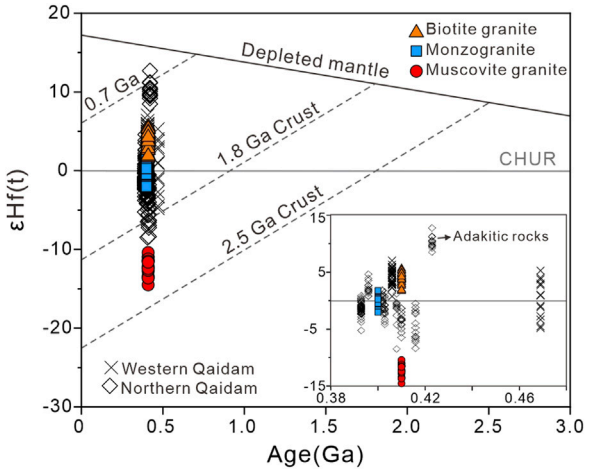

FIGURE 7
The plot of zircon εHf(t) values *vs.* U-Pb ages for investigated Huatugou granitoids, compared with published data of early Paleozoic granitoids in western and northern Qaidam (Song et al., 2014; Wu et al., 2014b; and Sun et al., 2020).

The biotite granite has positive zircon εHf(t) values of +1.7 to +5.6 (Figure 7), indicating that melted crustal igneous rocks were derived from juvenile materials. In addition, the high-temperature melting condition for producing A-type magma implies residual sources with an additional heat input from the mantle, which was encountered within the lower continental crust (Clemens et al., 1986). Therefore, the magmas of the biotite and monzogranites in the Huatugou area were generated by the partial melting of the lower continental crust under high-temperature and low-pressure conditions and underwent an AFC process during emplacement.

5.1.2 Muscovite granites

The muscovite granites are peraluminous granites (A/CNK=1.07–1.19) with 5%–7% muscovite and >1% CIPW normative corundum. Similar to typical S-type granite (Chappell and White, 2001), the muscovite granites exhibit high contents of SiO_2 (>72 wt%), K_2O (4.7–6.5 wt%), Rb (≥200 ppm), and Pb (36–51 ppm), and low contents of CaO (<1 wt%) and Sr (<30 ppm). With increasing SiO_2, P_2O_5 increases and Pb decreases (Figures 9G, H), typical S-type granite trends (Chappell and White, 2001). The muscovite granites are fractionated granites, indicated by their high Rb/Sr ratios (8.2–10.4) and REE tetrad effect (Figure 4). Additionally, Th, La, and Y contents decrease with increasing Rb (Figure 9I). According to Chappell (1999), these chemical trends are typical in fractionated S-type granites, indicating the fractionation of biotite, plagioclase, and monazite (Figure 10). S-type granites are generally derived from sedimentary or supracrustal rocks (Chappell and White, 2001). The muscovite granites yielded low zircon saturation temperatures of 638–656°C (Watson and Harrison, 1983), consistent with low-temperature magmas. Combined with

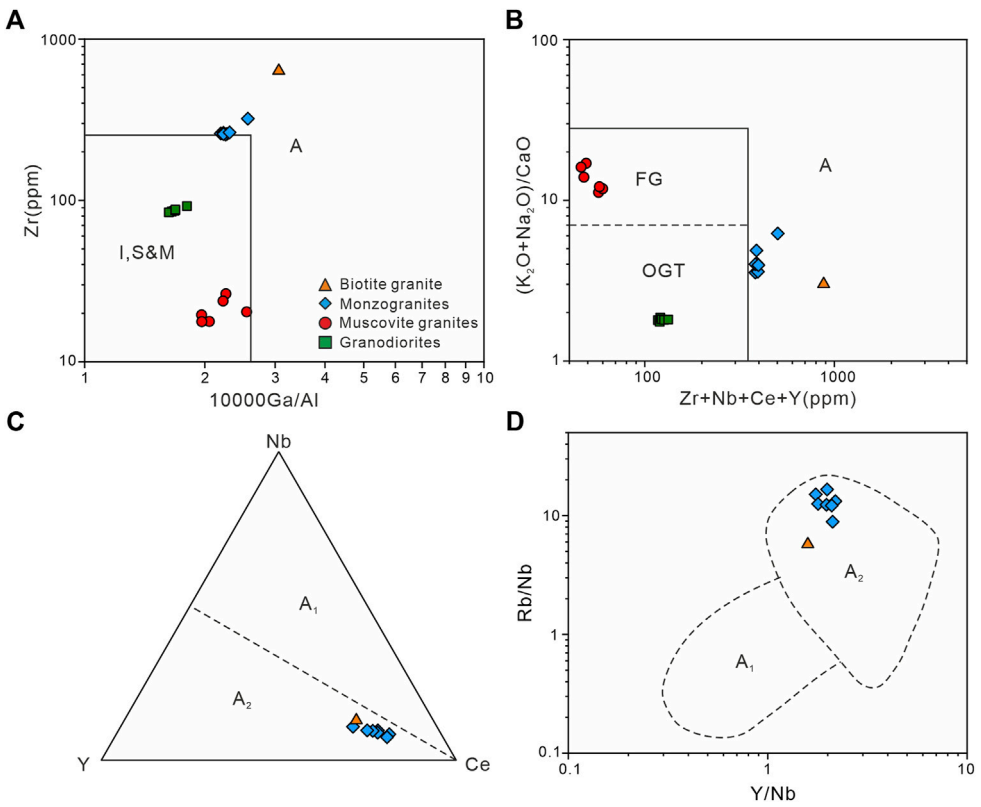

FIGURE 8
(A) Zr *vs.* 10000Ga/Al and **(B)** (Na_2O+K_2O)/CaO *vs.* Zr+Nb+Ce+Y discrimination diagrams (Whalen et al., 1987), indicating that the biotite granite and monzogranites in the Huatugou area are A-type granites. FG: Fractionated granites; OGT: unfractionated M-, I-, and S-type granites. **(C)** Nb-Y-Ce and **(D)** Rb/Nb *vs.* Y/Nb classification diagrams (Eby, 1992), where Huatugou biotite granite and monzogranites are plotted in the A_2 field.

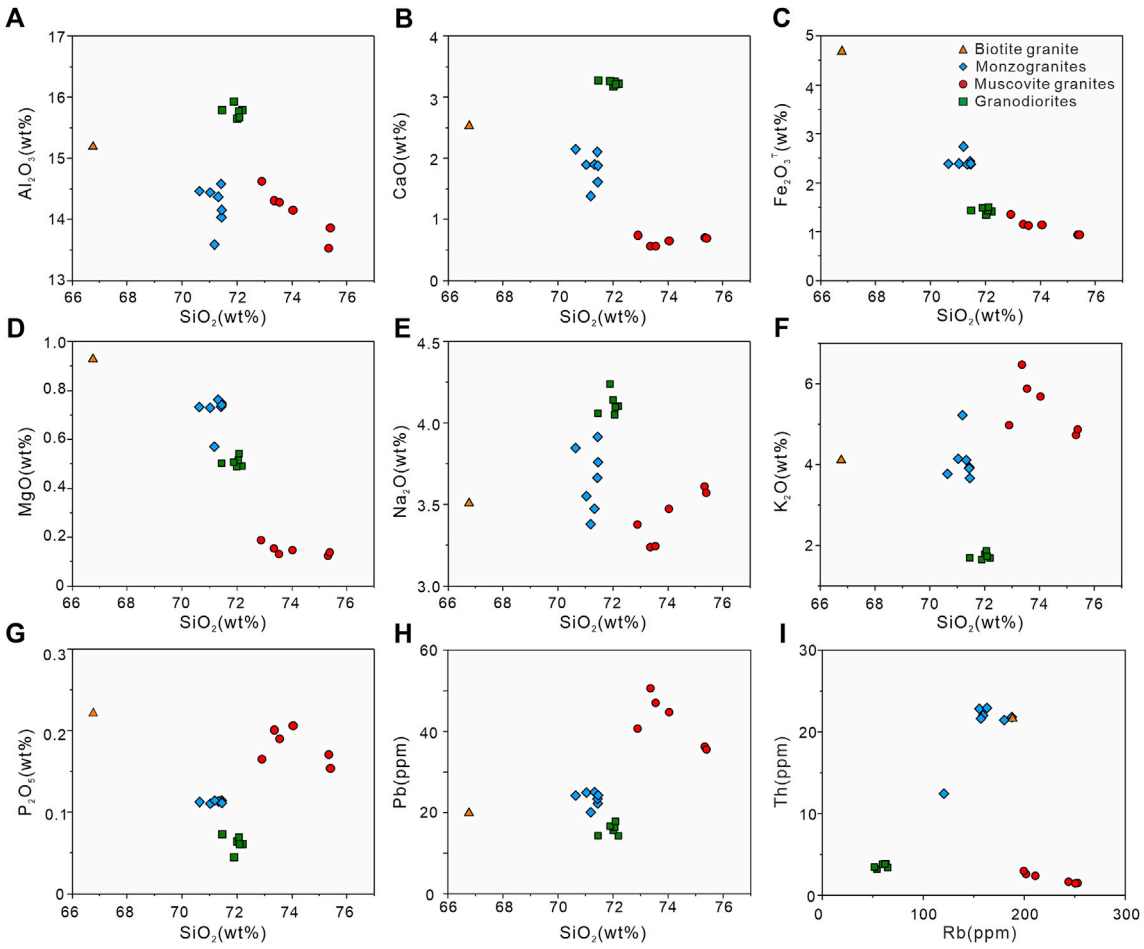

FIGURE 9
(A) Al_2O_3 *vs.* SiO_2, **(B)** CaO *vs.* SiO_2, **(C)** $Fe_2O_3^T$ *vs.* SiO_2, **(D)** MgO *vs.* SiO_2, **(E)** Na_2O *vs.* SiO_2, **(F)** K_2O *vs.* SiO_2, **(G)** P_2O_5 *vs.* SiO_2, **(H)** Pb *vs.* SiO_2, and **(I)** Rb *vs.* Th variation diagrams, showing that muscovite granites in the Huatugou area follow chemical trends of S-type proposed by Chappell (1999).

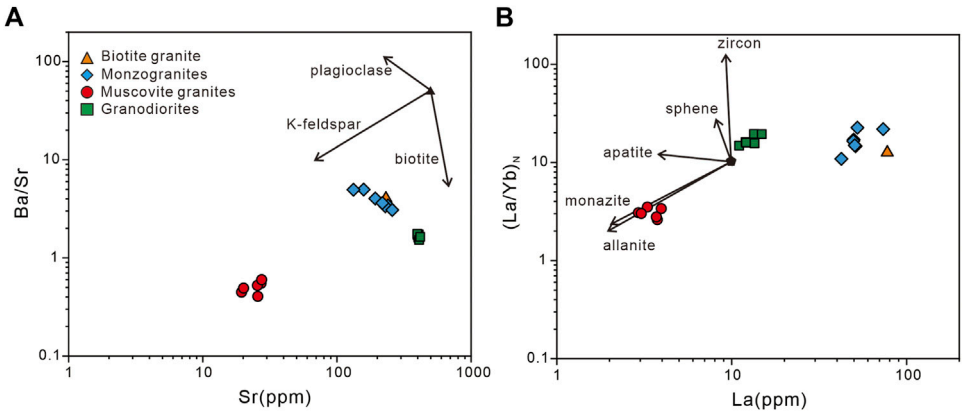

FIGURE 10
(A) Ba/Sr *vs.* Sr and **(B)** $(La/Yb)_N$ *vs.* La diagrams (Wu et al., 2003).

negative zircon εHf(t) values (−14.5 to −10.4, Figure 7), it is suggested that the magma of the muscovite granites resulted from the low-temperature partial melting of ancient crustal materials.

5.1.3 Granodiorites

The granodiorites are magnesian calcic granitoids characterized by high contents of Al_2O_3 (>15wt%) and Na_2O (>4 wt%) with low K_2O/

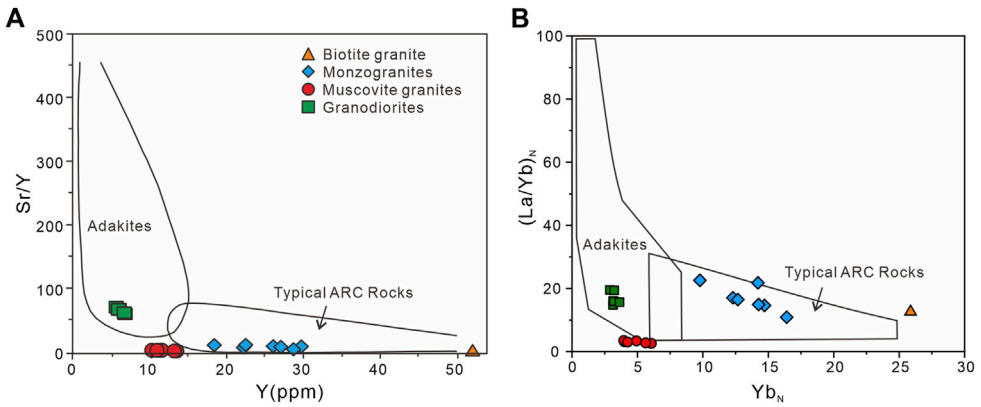

FIGURE 11
(A) Sr/Y *vs.* Y and **(B)** $(La/Yb)_N$ *vs.* Yb_N discrimination diagrams (Defant and Drummond, 1990; Martin, 1999), indicating that granodiorites in the Huatugou area are adakitic rocks.

Na_2O ratios (0.39–0.46). As to trace elements, the granodiorites exhibit strongly fractionated REE patterns ($(La/Yb)_N$=(15–20), low Y (6–7 ppm), and high Sr (398–418 ppm) and Sr/Y ratios (61–72), which are distinctive chemical features of adakitic rocks (Figure 11; Defant and Drummond, 1990; Martin, 1999). These adakitic affinities, combined with high CaO (3.18–3.29 wt%) and insignificant Eu anomalies (Figure 4A), imply that the garnet was stable and plagioclase was unstable in the source, indicative of a high-pressure condition.

The generation of adakitic rocks may have different mechanisms, including partial melting of the subducted oceanic slab with or without the involvement of mantle peridotite, partial melting of mafic lower crust with or without the participation of mantle peridotite, and fractional crystallization of arc basaltic magma (Castillo, 2012 and references therein). The high Ba contents (623–705 ppm), low Rb/Sr ratios (<0.2), and the absence of correlations between SiO_2 and other major oxides (Figure 9) of these granodiorites, indicate no or insignificant fractionation. Hence, the fractional crystallization model is largely ruled out. The granodiorites display consistently high SiO_2 (71.46–72.2 wt%) and low MgO (0.49–0.54 wt%) contents with high Fe* (0.71–0.73), inconsistent with the chemical signatures of mantle peridotite or mantle-derived magma. The granodiorites have zircons that contain Proterozoic cores and display complex growth patterns (Figure 5D). These zircon cores show chondrite-normalized REE patterns similar to (re) crystallized zircons (Figure 6H), indicating that they were captured in the source. Since there were ancient continental materials in the source, we favor the partial melting of the lower mafic crust over the oceanic slab to generate the granodiorites.

5.2 Granitic magmatism in the western Qaidam

The investigated Huatugou granitoids in this study, including granodiorites, muscovite granites, biotite granite, and monzogranites, yield weighted mean $^{206}Pb/^{238}U$ ages of 451 ± 6, 410 ± 6, 410 ± 3, and 400 ± 4 Ma (Figure 6). Dated zircons are euhedral and oscillatory-zoned with most Th/U ratios of > 0.5 (except the granodiorites), indicating a magmatic origin (Corfu 2003; Hoskin, 2003). For granodiorite zircons, the variations in Th/U ratios (0.07–0.40) might be due to disequilibrium crystallization (Wang et al., 2011). Hence, the weighted mean $^{206}Pb/^{238}U$ ages are interpreted as the timing of granitic magma crystallization, suggesting that the Huatugou granitoids were mainly emplaced during the late Ordovician-early Devonian. This study, combined with published U-Pb data (Figure 1B; Cheng et al., 2017; Wang C. et al., 2014a; Wu C. L. et al., 2014b), indicates that the western Qaidam block experienced multiple felsic magmatic events during 469–381 Ma (Figure 1B), mainly at 469–460 Ma, 453–440 Ma, and 411–400 Ma. The first granitic magmatism (469 to 460 Ma) is characterized by quartz diorite, diorite, and granite with zircon εHf(t) values varying from −4.8 to +5.3 (Figure 7; Wu C. L. et al., 2014b; Cheng et al., 2017), indicative of variations in melted sources.

The second granitic magmatism (453–440 Ma) formed granodiorite and granite with mylonitic textures (Cheng et al., 2017, this study), reflecting a syn-tectonic origin. In this study, the granodiorites exhibit adakitic features (Figure 11), and their magmas were generated by the partial melting of the lower mafic crust under high-pressure conditions. Similar granodiorite was also reported in the Yusupuleke area, west of western Qaidam, which was thought to result from the partial melting of garnet amphibolite within the thickened lower crust (Wang C. et al., 2014a).

The third granitic magmatism (411–400 Ma) is characterized by A-type granitoids with minor S-type granites, including monzogranite, syenogranite, granodiorite, biotite granite, muscovite granite (Cheng et al., 2017; Wu et al., 2014b; this study). A-type granitoids mainly exhibit positive zircon εHf(t) values (Figure 7), suggesting that their high-temperature magmas were derived from juvenile crustal sources. In Huatugou, monzogranites show lower zircon εHf(t) values with more fractionated features than the biotite granite, resulting from an AFC process during the emplacement of A-type magmas. S-type granites, such as the Huatugou muscovite granites, have negative zircon εHf(t) values (Figure 7), and their magmas were produced by low-temperature (650°C) partial melting of ancient crustal materials and experienced fractionation process (Figure 9).

5.3 Tectonic implications

According to this study, the Huatugou granitoid comprises three types: adakitic rocks (451 Ma), S-type granites (410 Ma), and A_2-type granites (410–400 Ma). Both magmas of adakitic rocks and A-type granitoids were generated by the partial melting of the lower crust. Differently, adakitic rocks were crystallized from magma produced by the high-pressure remelting without significant fractionation, which implies a relatively fast emplacement within a thickened continental crust. The A-type granitic magma was generated under high-temperature and low-pressure partial melting conditions and experienced an AFC process during emplacement, indicating a relatively slow emplacement/cooling within a thinned continental crust. The thickness change from the thickened to the thinned continent suggests that the western Qaidam experienced a tectonic transition from compression to extension. Considering three magmatism pulses, as summarized in section 5.2, this transition likely occurred between 440 and 411 Ma.

During 445–423 Ma, parts of northern Qaidam experienced ultrahigh-pressure metamorphism related to continental subduction (Song et al., 2005; Yang et al., 2005; Zhang et al., 2010). As ultrahigh-pressure metamorphic rocks are now exposed to the surface, the exhumation of the subducted continental crust should start around the same time. Otherwise, with ongoing subduction, the exhumed rocks would record younger peak metamorphic ages. The exhumation of deeply subducted continental crust was thought to result from the detachment of the dense oceanic slab (Zhang et al., 2016). The slab breakoff also induced mantle upwelling, which heated the thickened lower crust to produce adakitic magmas under high-pressure granulite-facies conditions in the Dulan area, south of northern Qaidam (Yu et al., 2019). The emplacement of high-temperature A-type granitoids as early as 418 Ma (Chen et al., 2020), as well as mantled-derived mafic-ultramafic plutons during 424–406 Ma in the southern Qaidam (Peng et al., 2016; Song et al., 2016; Wang et al., 2016), indicates that the exhumation of the subducted continental slab was followed by post-collisional extension of the whole Qaidam block. The third granitic magmatism (411–400 Ma) in western Qaidam also occurred in this extensional regime.

Moreover, the Dulan adakitic rocks (433–423 Ma) exhibit positive zircon εHf(t) values of 8.5–12.7 (Figure 7; Song et al., 2014; Yu et al., 2019). The protoliths of melted high-pressure granulite-facies sources are ~470 Ma gabbroic rocks with an arc affinity, similar to gabbro dikes intruding the Tanjianshan Group metavolcanic rocks (514–465 Ma, Wu et al., 1987; Li et al., 1999; Yuan et al., 2002; Shi et al., 2004). On the one hand, the Tanjianshan Group was exposed to the east and north margins of the Qaidam Basin. Their existence implies that the Proto-Tethys Ocean commenced subducting under the Qaidam block before 514 Ma. On the other hand, in Huatugou, the northwest margin of Qaidam, the UHT metamorphic rocks were formed at 540–500 Ma (Teng et al., 2020). If the Huatugou UHT metamorphism was linked to a collisional event alone, as inferred from clockwise P-T paths with prograde high-pressure (>1.4 GPa) history, the scenario would contradict the oceanic subduction. Nevertheless, the Huatugou ultrahigh-temperature metamorphic rocks were suggested as the result of the late Pan-African UHT metamorphism during the final assembly of the Gondwana (Teng et al., 2020; Teng and Zhang, 2020). The Qaidam block on the margin of East Gondwana, as a continental arc, is in line with the subduction of the Proto-Tethys Ocean around the Gondwana. In this position, the tectonic processes controlling the UHT metamorphism of the western Qaidam block are more intriguing than proposed and deserve further investigation. Nevertheless, our study suggests that the thickened continental crust of the Qaidam block was likely sustained until the detachment of the subducted crust during the continental collision. The extension of the Qaidam block commenced at ~420 Ma, likely after the exhumation of ultrahigh-pressure metamorphic rocks in subduction-collision complex belts.

6 Conclusion

1) The Huatugou granitoids, including granodiorites, monzogranites, biotite granites, and muscovite granites, intruded the Qaidam Precambrian basements during 451–400 Ma.
2) The granodiorites (451 ± 6 Ma) have adakitic affinities, and their magmas were generated by high-pressure remelting of the lower mafic crust. The muscovite granites (410 ± 6 Ma) with negative zircon εHf(t) values of −14.5 to −10.4 resulted from the partial melting of ancient crustal materials and S-type granite fractionation. The biotite granite (410 ± 3 Ma) was crystalized from a high-temperature A-type magma with positive zircon εHf(t) of +1.7 to +5.6, which was generated by the partial melting of juvenile crustal rocks in an extensional setting. The magmas of monzogranites (400 ± 4 Ma) derived from the same source as that of the biotite granite but experienced an AFC process during emplacement.
3) Combined with former studies, it is inferred that the Qaidam block consisted of the thickened continental crust during subduction processes until the detachment of subducted crust during the continental collision. The regional extension of the Qaidam block commenced at ~420 Ma, likely after the exhumation of ultrahigh-pressure metamorphic rocks in subduction-collision complex belts.

Data availability statement

The original contributions presented in the study are included in the article/Supplementary Material, further inquiries can be directed to the corresponding author.

Author contributions

XT and JZ contributed to the conception and design of the study. XT, XM, YW, and QG contributed to the acquisition and analysis of data. XT wrote the first draft of the manuscript. All authors contributed to the manuscript revision, and read, and approved the submitted version.

Funding

This work was financially supported by the National Natural Science Foundation of China (Grant nos. 41630207 and 42072237)

and the Geological Survey Project of China (Grant no. DD20221649).

Acknowledgments

We thank handling editor Meng Wang and two reviewers for constructive comments and suggestions to improve the manuscript.

Conflict of interest

The authors declare that the research was conducted in the absence of any commercial or financial relationships that could be construed as a potential conflict of interest.

Publisher's note

Supplementary material

The Supplementary Material for this article can be found online at: https://www.frontiersin.org/articles/10.3389/feart.2023.1105992/full#supplementary-material

References

Acosta-Vigil, A., London, D., and Morgan, G. B. (2006). Experiments on the kinetics of partial melting of a leucogranite at 200 MPa H_2O and 690–800°C: compositional variability of melts during the onset of H_2O-saturated crustal anatexis. *Contrib. to Mineral. Petrol.* 151 (5), 539–557. doi:10.1007/s00410-006-0081-8

Castillo, P. R. (2012). Adakite petrogenesis. *Lithos* 134-135, 304–316. doi:10.1016/j.lithos.2011.09.013

Castro, A., Douce, A. E. P., Corretge, L. G., de la Rosa, J. D., El-Biad, M., and El-Hmidi, H. (1999). Origin of peraluminous granites and granodiorites, iberian massif, Spain: an experimental test of granite petrogenesis. *Contrib. Mineral. Petrol.* 135 (2-3), 255–276. doi:10.1007/s004100050511

Chappell, B. W., and White, A. J. R. (2001). Two contrasting granite types: 25 years later. *Aust. J. Earth Sci.* 48 (4), 489–499. doi:10.1046/j.1440-0952.2001.00882.x

Chappell, B. W. (1999). Aluminium saturation in I- and S-type granites and the characterization of fractionated haplogranites. *Lithos* 46 (3), 535–551. doi:10.1016/s0024-4937(98)00086-3

Chen, H. W., Luo, Z. H., Mo, X. X., Zhang, X. T., Wang, J., and Wang, B. Z. (2006). SHRIMP ages of Kayakedengtage complex in the East Kunlun Mountains and their geological implications. *Acta Petrol. Mineral.* 25, 25–32. [in Chinese with English abstract].

Chen, D. L., Liu, L., Sun, Y., and Liou, J. G. (2009). Geochemistry and zircon U–Pb dating and its implications of the Yukahe HP/UHP terrane, the North Qaidam, NW China. *J. Asian Earth Sci.* 35 (3-4), 259–272. doi:10.1016/j.jseaes.2008.12.001

Chen, J., Fu, L., Wei, J., Selby, D., Zhang, D., Zhou, H., et al. (2020). Proto-tethys magmatic evolution along northern Gondwana: Insights from late silurian–middle devonian A-type magmatism, East Kunlun orogen, northern Tibetan plateau, China. *Lithos* 356-357, 105304. doi:10.1016/j.lithos.2019.105304

Cheng, F., Jolivet, M., Hallot, E., Zhang, D. W., Zhang, C. H., and Guo, Z. J. (2017). Tectono-magmatic rejuvenation of the Qaidam craton, northern Tibet. *Gondwana Res.* 49, 248–263. doi:10.1016/j.gr.2017.06.004

Collins, W. J., Beams, S. D., White, A. J. R., and Chappell, B. W. (1982). Nature and origin of A-type granites with particular reference to southeastern Australia. *Contrib. to Mineral. Petrol.* 80 (2), 189–200. doi:10.1007/BF00374895

Clemens, J. D., Holloway, J. R., and White, A. J. R. (1986). Origin of an A-type granite; experimental constraints. *Am. Mineral.* 71 (3-4), 317–324.

Corfu, F. (2003). Atlas of zircon textures. *Rev. Mineral. Geochem.* 53 (1), 469–500. doi:10.2113/0530469

Defant, M. J., and Drummond, M. S. (1990). Derivation of some modern arc magmas by melting of young subducted lithosphere. *Nature* 347 (6294), 662–665. doi:10.1038/347662a0

Dong, Y. P., He, D. F., Sun, S. S., Liu, X. M., Zhou, X. H., Zhang, F. F., et al. (2018). Subduction and accretionary tectonics of the East Kunlun orogen, Western segment of the central China orogenic system. *Earth-Sci. Rev.* 186, 231–261. doi:10.1016/j.earscirev.2017.12.006

Eby, G. N. (1992). Chemical subdivision of the A-type granitoids: Petrogenetic and tectonic implications. *Geology* 20 (7), 641–644. doi:10.1130/0091-7613(1992)020<0641:csotat>2.3.co;2

Frost, B. R., Barnes, C. G., Collins, W. J., Arculus, R. J., Ellis, D. J., and Frost, C. D. (2001). A geochemical classification for granitic rocks. *J. Petrol.* 42 (11), 2033–2048. doi:10.1093/petrology/42.11.2033

He, D., Dong, Y., Zhang, F., Yang, Z., Sun, S., Cheng, B., et al. (2016). The 1.0Ga S–type granite in the East Kunlun orogen, northern Tibetan plateau: Implications for the meso– to neoproterozoic tectonic evolution. *J. Asian Earth Sci.* 130, 46–59. doi:10.1016/j.jseaes.2016.07.019

He, D., Dong, Y., Liu, X., Zhou, X., Zhang, F., and Sun, S. (2018). Zircon U–Pb geochronology and Hf isotope of granitoids in East Kunlun: Implications for the neoproterozoic magmatism of Qaidam block, northern Tibetan plateau. *Precambrian Res.* 314, 377–393. doi:10.1016/j.precamres.2018.06.017

He, F., Song, S. G., and ShuGuang, S. (2020). The grenvillian-aged UHT granulite in Jinshuikou region, East Kunlun orogenic belt. *Acta Petrol. Sin.* 36, 1030–1040. [in Chinese with English abstract]. doi:10.18654/1000-0569/2020.04.04

He, D., Dong, Y., Hauzenberger, C. A., Sun, S., Neubauer, F., Zhou, B., et al. (2022). Neoproterozoic HP granulite and its tectonic implication for the East Kunlun orogen, northern Tibetan plateau. *Precambrian Res.* 378, 106778. doi:10.1016/j.precamres.2022.106778

Hopkinson, T., Harris, N., Roberts, N. M. W., Warren, C. J., Hammond, S., Spencer, C. J., et al. (2019). Evolution of the melt source during protracted crustal anatexis: An example from the Bhutan Himalaya. *Geology* 48 (1), 87–91. doi:10.1130/g47078.1

Hoskin, P. W. O. (2003). The composition of zircon and igneous and metamorphic petrogenesis. *Rev. Mineral. Geochem.* 53 (1), 27–62. doi:10.2113/0530027

Irvine, T. N., and Baragar, W. R. A. (1971). A guide to the chemical classification of the common volcanic rocks. *Can. J. Earth Sci.* 8 (5), 523–548. doi:10.1139/e71-055

Jackson, S. E., Pearson, N. J., Griffin, W. L., and Belousova, E. A. (2004). The application of laser ablation-inductively coupled plasma-mass spectrometry to *in situ* U–Pb zircon geochronology. *Chem. Geol.* 211 (1-2), 47–69. doi:10.1016/j.chemgeo.2004.06.017

Li, H. K., Lu, S. N., Zhao, F. Q., Li, H. M., Yu, H. F., and Zheng, J. K. (1999). Geochronological framework of the Neoproterozoic major geological events in the northern margin of the Qaidam basin. *Geoscience* (2), 224–225. [in Chinese].

Liu, Y. S., Gao, S., Hu, Z. C., Gao, C. G., Zong, K. Q., and Wang, D. B. (2010). Continental and oceanic crust recycling-induced melt-peridotite interactions in the trans-north China orogen: U-Pb dating, Hf isotopes and trace elements in zircons from mantle xenoliths. *J. Petrol.* 51 (1-2), 537–571. doi:10.1093/petrology/egp082

Lu, L., Wu, Z. H., Hu, D. G., Barosh, P. J., Hao, S., and Zhou, C. J. (2010). Zircon U-Pb age for rhyolite of the Maoniushan Formation and its tectonic significance in the East Kunlun Mountains. *Acta Petrol. Sin.* 26, 1150–1158. [in Chinese with English abstract].

Ludwig, K. (2012). *User's manual for Isoplot 3.75: A geochronological toolkit for microsoft excel*. Berkley: Berkley Geochronological Centre, Special Publication 5.

Maniar, P. D., and Piccoli, P. M. (1989). Tectonic discrimination of granitoids. *GSA Bull.* 101 (5), 635–643. doi:10.1130/0016-7606(1989)101<0635:tdog>2.3.co;2

Martin, H. (1999). Adakitic magmas: Modern analogues of archaean granitoids. *Lithos* 46 (3), 411–429. doi:10.1016/s0024-4937(98)00076-0

Mattinson, C. G., Wooden, J. L., Liou, J. G., Bird, D. K., and Wu, C. L. (2006). Age and duration of eclogite-facies metamorphism, North Qaidam HP/UHP terrane, Western China. *Am. J. Sci.* 306 (9), 683–711. doi:10.2475/09.2006.01

Meng, F. C., Zhang, J. X., and Cui, M. H. (2013). Discovery of early paleozoic eclogite from the East Kunlun, western China and its tectonic significance. *Gondwana Res.* 23 (2), 825–836. doi:10.1016/j.gr.2012.06.007

Middlemost, E. A. K. (1994). Naming materials in the magma/igneous rock system. *Earth-Sci. Rev.* 37 (3), 215–224. doi:10.1016/0012-8252(94)90029-9

Patiño Douce, A. E., and Harris, N. (1998). Experimental constraints on himalayan anatexis. *J. Petrol.* 39 (4), 689–710. doi:10.1093/petroj/39.4.689

Patiño Douce, A. E. (1995). Experimental generation of hybrid silicic melts by reaction of high-Al basalt with metamorphic rocks. *J. Geophys. Res. Solid Earth* 100 (B8), 15623–15639. doi:10.1029/94jb03376

Peng, B., Sun, F., Li, B., Wang, G., Li, S., Zhao, T., et al. (2016). The geochemistry and geochronology of the Xiarihamu II mafic–ultramafic complex, Eastern Kunlun, Qinghai Province, China: Implications for the Genesis of magmatic Ni–Cu sulfide deposits. *Ore Geol. Rev.* 73, 13–28. doi:10.1016/j.oregeorev.2015.10.014

Ren, Y., Chen, D., Zhu, X., Ren, Z., Gong, X., and Luo, F. (2019). Two orogenic cycles recorded by eclogites in the Yuka–Luofengpo terrane: Implications for the Mesoproterozoic to early Paleozoic tectonic evolution of the North Qaidam orogenic belt, NW China. *Precambrian Res.* 333, 105449. doi:10.1016/j.precamres.2019.105449

Ren, Y., Chen, D., Wang, H., Zhu, X., and Bai, B. (2021). Grenvillian and early Paleozoic polyphase metamorphism recorded by eclogite and host garnet mica schist in the North Qaidam orogenic belt. *Geosci. Front.* 12 (4), 101170. doi:10.1016/j.gsf.2021.101170

Shi, R. D., Yang, J. S., Wu, C. L., Iizuka, T., and Hirata, T. (2004). Island arc volcanic rocks in the North Qaidam UHP metamorphic Belt. *Acta Geol. Sin.* 78, 52–64. [in Chinese with English abstract].

Sláma, J., Košler, J., Condon, D. J., Crowley, J. L., Gerdes, A., Hanchar, J. M., et al. (2008). Plešovice zircon — a new natural reference material for U–Pb and Hf isotopic microanalysis. *Chem. Geol.* 249 (1-2), 1–35. doi:10.1016/j.chemgeo.2007.11.005

Song, S. G., Zhang, L. F., Niu, Y. L., Su, L., Jian, P., and Liu, D. Y. (2005). Geochronology of diamond-bearing zircons from garnet peridotite in the north Qaidam UHPM belt, northern Tibetan plateau: A record of complex histories from oceanic lithosphere subduction to continental collision. *Earth Planet. Sci. Lett.* 234 (1-2), 99–118. doi:10.1016/j.epsl.2005.02.036

Song, S. G., Su, L., Li, X. H., Zhang, G. B., Niu, Y. L., and Zhang, L. F. (2010). Tracing the 850-Ma continental flood basalts from a piece of subducted continental crust in the North Qaidam UHPM belt, NW China. *Precambrian Res.* 183 (4), 805–816. doi:10.1016/j.precamres.2010.09.008

Song, S. G., Niu, Y. L., Su, L., Wei, C. J., and Zhang, L. F. (2014). Adakitic (tonalitic-trondhjemitic) magmas resulting from eclogite decompression and dehydration melting during exhumation in response to continental collision. *Geochim. Cosmochim. Acta* 130, 42–62. doi:10.1016/j.gca.2014.01.008

Song, X. Y., Yi, J. N., Chen, L. M., She, Y. W., Liu, C. Z., Dang, X. Y., et al. (2016). The giant xiarihamu Ni-Co sulfide deposit in the East Kunlun orogenic belt, northern tibet plateau, China. *Econ. Geol.* 111 (1), 29–55. doi:10.2113/econgeo.111.1.29

Song, S., Bi, H., Qi, S., Yang, L., Allen, M. B., Niu, Y., et al. (2018). HP–UHP metamorphic belt in the East Kunlun orogen: Final closure of the Proto-Tethys Ocean and formation of the pan-north-China continent. *J. Petrol.* 59 (11), 2043–2060. doi:10.1093/petrology/egy089

Sun, S. S., and McDonough, W. F. (1989). Chemical and isotopic systematics of oceanic basalts: Implications for mantle composition and processes. *Geol. Soc. Lond. Spec. Publ.* 42 (1), 313–345. doi:10.1144/gsl.sp.1989.042.01.19

Sun, G. C., Gao, P., Zhao, Z. F., and Zheng, Y. F. (2020). Syn-exhumation melting of the subducted continental crust: Geochemical evidence from early Paleozoic granitoids in North Qaidam, northern Tibet. *Lithos* 374-375, 105707–106375. doi:10.1016/j.lithos.2020.105707

Taylor, S. R., and McLennan, S. M. (1995). The geochemical evolution of the continental crust. *Rev. Geophys.* 33 (2), 241–265. doi:10.1029/95rg00262

Teng, X., Zhang, J. X., and JianXin, Z. (2020). Ultrahigh temperature metamorphism in collisional orogen and its tectonic significance: An example from the Pan-African orogens. *Acta Petrol. Sin.* 36 (10), 2963–2982. [in Chinese with English abstract]. doi:10.18654/1000-0569/2020.10.03

Teng, X., Zhang, J., Mao, X., Lu, Z., and Zhou, G. (2020). The earliest cambrian UHT metamorphism in the Qaidam block, Western China: A record of the final assembly of greater Gondwana? *Gondwana Res.* 87, 118–137. doi:10.1016/j.gr.2020.06.009

Teng, X., Zhang, J., Mao, X., Lu, Z., Zhou, G., Wu, Y., et al. (2022). Qaidam block situated in the interior of Rodinia and Gondwana: New magmatic and metamorphic constraints. *Precambrian Res.* 381, 106866. doi:10.1016/j.precamres.2022.106866

Wang, Y. S., Zhuang, Q. X., and Shi, C. Y. (1983). *The precambrian feature of qinghai" in contribution to the geology of the qinghai-xizang (tibet) plateau (2).* Beijing: Geological Publishing House, 56–69. [in Chinese with English abstract].

Wang, X., Griffin, W. L., Chen, J., Huang, P., and Li, X. (2011). U and Th contents and Th U ratios of zircon in felsic and mafic magmatic rocks: Improved zircon-melt distribution coefficients. *Acta Geol. Sin.* 85 (1), 164–174. doi:10.1111/j.1755-6724.2011.00387.x

Wang, C., Liu, L., Xiao, P. X., Cao, Y. T., Yu, H. Y., Meert, J. G., et al. (2014a). Geochemical and geochronologic constraints for Paleozoic magmatism related to the orogenic collapse in the Qimantagh–South Altyn region, northwestern China. *Lithos* 202-203, 1–20. doi:10.1016/j.lithos.2014.05.016

Wang, G., Sun, F. Y., Li, B. L., Li, S. J., Zhao, J. W., Ao, Z., et al. (2014b). Petrography, zircon U-Pb geochronology and geochemistry of the mafic-ultramafic intrusion in Xiarihamu Cu-Ni deposit from East Kunlun, with implications for geodynamic setting. *Earth Sci. Front.* 21, 381–401. [in Chinese with English abstract].

Wang, G., Sun, F., Li, B., Ao, C., Li, S., Zhao, J., et al. (2016). Geochronology, geochemistry and tectonic implication of Early Neoproterozoic monzogranite in Xiarihamu ore district from East Kunlun. *Geotect. Metallog.* 40, 1247–1260. [in Chinese with English abstract].

Watson, E. B., and Harrison, T. M. (1983). Zircon saturation revisited - temperature and composition effects in a variety of crustal magma types. *Earth Planet. Sci. Lett.* 64 (2), 295–304. doi:10.1016/0012-821x(83)90211-x

Whalen, J. B., Currie, K. L., and Chappell, B. W. (1987). A-type granites: geochemical characteristics, discrimination and petrogenesis. *Contrib. Mineral. Petrol.* 95 (4), 407–419. doi:10.1007/bf00402202

Wiedenbeck, M., AllÉ, P., Corfu, F., Griffin, W. L., Meier, M., Oberli, F., et al. (1995). Three natural zircon standards for U-Th-Pb, Lu-Hf, trace element and REE analyses. *Geostand. Geoanal. Res.* 19 (1), 1–23. doi:10.1111/j.1751-908x.1995.tb00147.x

Winther, K. T. (1996). An experimentally based model for the origin of tonalitic and trondhjemitic melts. *Chem. Geol.* 127 (1-3), 43–59. doi:10.1016/0009-2541(95)00087-9

Wu, J. R., Ren, B. S., Zhang, M., Gao, D. C., Zhao, T., Zhang, H. W., et al. (1987). The genetic type and geological characteristics of the Xitieshan massive sulphide deposit, Qinghai. *Bull. Xi'an Inst. Geol. Mineral Resour. Chin. Acad. Geol. Sci.* (20), 1–81. [in Chinese with English abstract].

Wu, F. Y., Jahn, B. M., Wilde, S. A., Lo, C. H., Yui, T. F., Lin, Q., et al. (2003). Highly fractionated I-type granites in NE China (I): geochronology and petrogenesis. *Lithos* 66 (3), 241–273. doi:10.1016/s0024-4937(02)00222-0

Wu, C., Gao, Y., Li, Z., Lei, M., Qin, H., Li, M., et al. (2014a). Zircon SHRIMP U-Pb dating of granites from Dulan and the chronological framework of the North Qaidam UHP belt, NW China. *Sci. China Earth Sci.* 57 (12), 2945–2965. doi:10.1007/s11430-014-4958-5

Wu, C. L., Gao, Y. H., Lei, M., Qin, H. P., Liu, C. H., Li, M. Z., et al. (2014b). Zircon SHRIMP U-Pb dating, Lu-Hf isotopic characteristics and petrogenesis of the Palaeozoic granites in Mangya area, southern Altun, NW China. *Acta Petrol. Sin.* 30 (8), 2297–2323. [in Chinese with English abstract].

Wu, F. Y., Liu, X. C., Ji, W. Q., Wang, J. M., and Yang, L. (2017). Highly fractionated granites: Recognition and research. *Sci. China Earth Sci.* 60, 1201–1219. doi:10.1007/s11430-016-5139-1

Yang, J. S., Liu, F. L., Wu, C. L., Xu, Z. Q., Shi, R. D., Chen, S. Y., et al. (2005). Two ultrahigh-pressure metamorphic events recognized in the Central Orogenic Belt of China: Evidence from the U-Pb dating of coesite-bearing zircons. *Int. Geol. Rev.* 47 (4), 327–343. doi:10.2747/0020-6814.47.4.327

Yang, S., Su, L., Song, S., Allen, M. B., Feng, D., Wang, M., et al. (2020). Melting of subducted continental crust during collision and exhumation: Insights from granitic rocks from the North Qaidam UHP metamorphic belt, NW China. *Lithos* 378-379, 105794–106379. doi:10.1016/j.lithos.2020.105794

Yu, S., Zhang, J., del Real, P. G., Zhao, X., Hou, K., Gong, J., et al. (2013). The Grenvillian orogeny in the Altun–Qilian–North Qaidam mountain belts of northern Tibet Plateau: Constraints from geochemical and zircon U–Pb age and Hf isotopic study of magmatic rocks. *J. Asian Earth Sci.* 73, 372–395. doi:10.1016/j.jseaes.2013.04.042

Yu, S., Zhang, J., Li, S., Santosh, M., Li, Y., Liu, Y., et al. (2019). TTG-Adakitic-Like (Tonalitic-Trondhjemitic) magmas resulting from partial melting of metagabbro under high-pressure condition during continental collision in the north Qaidam UHP terrane, western China. *Tectonics* 38 (3), 791–822. doi:10.1029/2018tc005259

Yuan, G. B., Wang, H. C., Li, H. M., Hao, G. J., Xin, H. T., Zhang, B. H., et al. (2002). Zircon U-Pb age of the gabbros in Luliangshan area on the Northern margin of Qaidam basin and its geological implication. *Prog. Precambrian Res.* 25, 36–40. [in Chinese with English abstract].

Zhang, J. X., Meng, F. C., and Wan, Y. S. (2003). Early Paleozoic tectono-thermal event of the Jinshuikou Grop on the southern margin of Qaidam: Zircon U-Pb SHRIMP age evidence. *Geol. Bull. China* 22 (6), 397–404. [in Chinese with English abstract].

Zhang, J. X., Mattinson, C. G., Yu, S. Y., Li, J. P., and Meng, F. C. (2010). U-Pb zircon geochronology of coesite-bearing eclogites from the southern dulan area of the north Qaidam UHP terrane, northwestern China: Spatially and temporally extensive UHP metamorphism during continental subduction. *J. Metamorph. Geol.* 28 (9), 955–978. doi:10.1111/j.1525-1314.2010.00901.x

Zhang, Z., Dong, X., Xiang, H., Liou, J. G., and Santosh, M. (2013). Building of the deep gangdese arc, south tibet: Paleocene plutonism and granulite-facies metamorphism. *J. Petrol.* 54 (12), 2547–2580. doi:10.1093/petrology/egt056

Zhang, L., Chen, R. X., Zheng, Y. F., Li, W. C., Hu, Z., Yang, Y., et al. (2016). The tectonic transition from oceanic subduction to continental subduction: Zirconological constraints from two types of eclogites in the North Qaidam orogen, northern Tibet. *Lithos* 244, 122–139. doi:10.1016/j.lithos.2015.12.003

Zhang, J. X., Yu, S. Y., and Mattinson, C. G. (2017). Early Paleozoic polyphase metamorphism in northern Tibet, China. *Gondwana Res.* 41, 267–289. doi:10.1016/j.gr.2015.11.009

Zhang, J. X., Lu, Z. L., Mao, X. H., Teng, X., Zhou, G. S., Wu, Y. W., et al. (2021). Revisiting the precambrian micro-continental blocks within the early paleozoic orogenic system of the northeastern qinghai-tibet plateau: Insight into the origin of Proto tethyan ocean. *Acta Petrol. Sin.* 37 (1), 74–94. [in Chinese with English abstract]. doi:10.18654/1000-0569/2021.01.06

Zhu, D. C., Wang, Q., Chung, S. L., Cawood, P. A., and Zhao, Z. D. (2018). Gangdese magmatism in southern tibet and India–asia convergence since 120 Ma. *Geol. Soc. Lond. Spec. Publ.* 483, 583–604. doi:10.1144/sp483.14